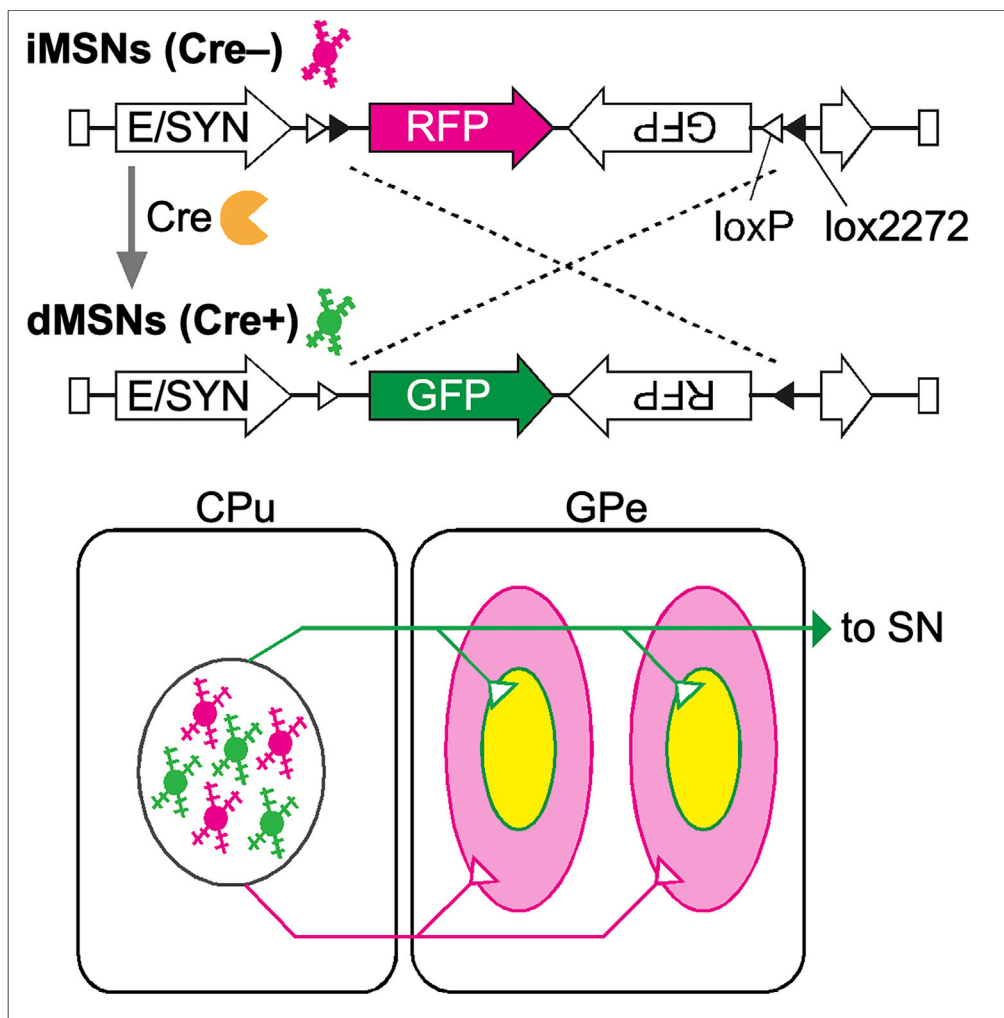## Article

Overlapping Projections of Neighboring Direct and Indirect Pathway Neostriatal Neurons to Globus Pallidus External Segment

Shinichiro Okamoto, Jaerin Sohn, Takuma Tanaka, ..., Masato Koike, Fumino Fujiyama, Hiroyuki Hioki

h-hioki@juntendo.ac.jp

HIGHLIGHTS
Neighboring dMSNs and iMSNs were exclusively labeled with GFP and RFP

dMSNs and iMSNs formed two axonal arborizations in the GPe in a topographic manner

Axonal arborizations of dMSNs were embedded within the arborizations of iMSNs

The centers of projections from neighboring dMSNs and iMSNs were almost overlapped

iScience

Article

Overlapping Projections of Neighboring Direct and Indirect Pathway Neostriatal Neurons to Globus Pallidus External Segment

Shinichiro Okamoto,[1,2,3] Jaerin Sohn,[4] Takuma Tanaka,[5] Megumu Takahashi,[1,3] Yoko Ishida,[1] Kenta Yamauchi,[1,2] Masato Koike,[1,2] Fumino Fujiyama,[6] and Hiroyuki Hioki[1,7,*]

SUMMARY

Indirect pathway medium-sized spiny neurons (iMSNs) in the neostriatum are well known to project to the external segment of the globus pallidus (GPe). Although direct MSNs (dMSNs) also send axon collaterals to the GPe, it remains unclear how dMSNs and iMSNs converge within the GPe. Here, we selectively labeled neighboring dMSNs and iMSNs with green and red fluorescent proteins using an adeno-associated virus vector and examined axonal projections of dMSNs and iMSNs to the GPe in mice. Both dMSNs and iMSNs formed two axonal arborizations displaying topographical projections in the dorsoventral and mediolateral planes. iMSNs displayed a wider and denser axon distribution, which included that of dMSNs. Density peaks of dMSN and iMSN axons almost overlapped, revealing convergence of dMSN axons in the center of iMSN projection fields. These overlapping projections suggest that dMSNs and iMSNs may work cooperatively via interactions within the GPe.

INTRODUCTION

The neostriatum, caudate-putamen (CPu), is the major input nucleus of the basal ganglia, which plays a key role in motor control (Albin et al., 1989; DeLong, 1990) and receives excitatory inputs mainly from the cerebral cortex and thalamus (Alexander and Crutcher, 1990). Medium-sized spiny neurons (MSNs), projection neurons in the CPu, send information to the external segment of the globus pallidus (GPe), entopeduncular nucleus (EP; rodent homolog of the internal segment of the primate globus pallidus), and substantia nigra pars reticulata (SNr), the latter two structures being output nuclei of the basal ganglia (Alexander and Crutcher, 1990). Unraveling the characteristics of these neurons and their axonal distributions that relay information from the upstream to the downstream nuclei is crucial for understanding the function of the basal ganglia.

Projections from the CPu can be divided into two distinct pathways: direct pathway neurons (dMSNs) target the EP and SNr directly, whereas indirect pathway neurons (iMSNs) project to the GPe, and GPe neurons then send axons to the output nuclei via the subthalamic nucleus (Alexander and Crutcher, 1990). In the traditional model of the basal ganglia, direct and indirect pathways have been considered to play opposing roles: the direct pathway delivers a "go signal" for action promotion, whereas the indirect pathway sends a "no-go signal" to suppress movement (Albin et al., 1989; DeLong, 1990). However, accumulating evidence supports coordinated interactions between the direct and indirect pathways (Peak et al., 2019; Tecuapetla et al., 2014): for example, dMSNs and iMSNs can be cooperatively activated during motor action initiation (Cui et al., 2013). These findings indicate that the direct and indirect pathways are not always competing but that a structural basis for the coordinated functions of dMSNs and iMSNs may underlie motor control by the basal ganglia.

dMSNs and iMSNs mainly project to different nuclei in the basal ganglia, but it has been reported that their outputs converge in the GPe. Although dMSNs project predominantly to the EP and SNr, several studies have revealed that dMSNs have axon collaterals in the GPe (Fujiyama et al., 2011; Kawaguchi et al., 1990; Wu et al., 2000). Indeed, an electrophysiological study has revealed that both iMSNs and dMSNs inhibit the activity of GPe neurons (Cazorla et al., 2014). Although the inhibitory effect of both dMSNs and iMSNs on GPe neuron activity may partially contribute to their coordinated functions, the individual projection

[1]Department of Cell Biology and Neuroscience, Juntendo University Graduate School of Medicine, 2-1-1 Hongo, Bunkyo-ku, Tokyo 113-8421, Japan

[2]Advanced Research Institute for Health Sciences, Juntendo University, 2-1-1 Hongo, Bunkyo-ku, Tokyo 113-8421, Japan

[3]Department of Neuroscience, Graduate School of Medicine, Kyoto University, Yoshida-Konoe-cho, Sakyo-ku, Kyoto 606-8501, Japan

[4]Division of Cerebral Circuitry, National Institute for Physiological Sciences, 5-1 Higashiyama Myodaiji, Okazaki, Aichi 444-8787, Japan

[5]Graduate School of Data Science, Shiga University, 1-1-1 Banba, Hikone, Shiga 522-8522, Japan

[6]Laboratory of Neural Circuitry, Graduate School of Brain Science, Doshisha University, 1-3 Tatara Miyakodani, Kyotanabe, Kyoto 610-0394, Japan

[7]Lead Contact

*Correspondence: h-hioki@juntendo.ac.jp

https://doi.org/10.1016/j.isci.2020.101409

patterns of dMSNs and iMSNs remain to be clarified. Therefore, to understand how dMSNs and iMSNs cooperatively play a role in motor control, it might be essential to anatomically clarify the convergence of dMSN and iMSN axons in the GPe and identify the corresponding neural circuitry in the basal ganglia.

In the present study, we explored the precise distributions of the varicose fibers of dMSNs and iMSNs in the mouse GPe. We injected an adeno-associated virus (AAV) vector into the CPu of dopamine receptor D1 (Drd1)-Cre transgenic mice (Gong et al., 2007) and labeled dMSNs and iMSNs with green (GFP) and red fluorescent proteins (RFP), respectively. In addition, the palmitoylation signal sequence attached to GFP and RFP enables efficient visualization of axon fibers (Furuta et al., 2001; Kameda et al., 2008; Nishino et al., 2008). We quantitatively analyzed the convergence of dMSN and iMSN axon fibers in the GPe and found a unique distribution of dMSN axons in relation to the iMSN projections.

RESULTS

Selective Labeling of dMSNs and iMSNs

In order to label neostriatal neurons of the direct and indirect pathways with different fluorescent proteins, we applied the Cre-dependent recombination system with an AAV vector developed in this study and Cre-expressing transgenic mice. We first validated the specificity of Cre recombinase expression in dMSNs of Drd1-Cre transgenic mice using double immunofluorescence staining for Cre and chemical markers for dMSNs and iMSNs. MSNs are inhibitory GABAergic neurons and account for over 95% of neostriatal neurons (Graveland and DiFiglia, 1985; Rymar et al., 2004). dMSNs and iMSNs can be characterized based on their expression of chemical markers as well as their projection targets: dMSNs express Drd1 and prepro-dynorphin (PPD; the precursor protein of dynorphin), whereas iMSNs express dopamine receptor D2 (Drd2) and preproenkephalin (PPE) (Gerfen et al., 1990; Gerfen and Young, 1988; Le Moine and Bloch, 1995; Le Moine et al., 1990; Lee et al., 1997; Sonomura et al., 2007). We observed specific Cre recombinase expression in dMSNs in Drd1-Cre mice (Figures 1A and 1B). Almost all Cre-positive (+) neurons exhibited immunoreactivity for PPD (98.8%; 255 of 258 cells, n = 3 mice), and 95.5% of PPD+ neurons displayed immunoreactivity for Cre (255 of 267 cells) (Figure 1A). In contrast, only 3.6% of PPE+ neurons were immunoreactive for Cre (10 of 277 cells). Conversely, 3.6% of Cre+ neurons displayed immunoreactivity for PPE (10 of 280 cells) (Figure 1B).

We developed an AAV vector that expresses palmitoylation site-attached GFP (pG) or palmitoylation site-attached RFP (pR) in the presence or absence of Cre recombinase, respectively (Figure 1C). Focal injections of the AAV vector into the CPu of Drd1-Cre mice should thus label neighboring dMSNs and iMSNs with GFP and RFP, respectively. We tested the developed labeling system with immunofluorescence staining for GFP, RFP, PPD, and PPE in Drd1-Cre mice injected with the AAV vector. One week after injections, most GFP+ neurons were immunopositive for PPD (95.2%; 99 of 104 cells, n = 3 mice) and a few for PPE (2.9%; 3 of 101 cells). In contrast, most RFP+ neurons showed immunoreactivity for PPE (97.1%; 100 of 103 cells) but rarely for PPD (5.0%; 5 of 100 cells) (Figures 1D and 1E). In addition, both GFP+ and RFP+ neurons exhibited a high density of spines on their dendrites, a key feature of MSNs (Chang et al., 1981; Preston et al., 1980) (Figures 1D and 1E). These findings indicate that dMSNs and iMSNs were successfully labeled with GFP and RFP, respectively, following injections of the AAV vector into the CPu of Drd1-Cre transgenic mice.

Visualization of dMSN and iMSN Axon Fibers by Immunoperoxidase Staining

To visualize axon fibers with high sensitivity, we performed immunoperoxidase staining for GFP and RFP in mouse brain sections (n = 3 mice). In the CPu, strong immunoreactivities for GFP and RFP were observed in cell bodies, dendrites, and axons (Figures 2A and 2G). Furthermore, dense spines were clearly observed on their dendrites (Figures 2B and 2H). RFP+ aspiny neurons were occasionally observed (data not shown). These aspiny interneurons do not express Cre recombinase, and thus they were labeled with RFP when the present method was used. Given that axons of striatal interneurons remain within the CPu (Alexander and Crutcher, 1990), RFP+ axon fibers outside the CPu must originate from iMSNs in the CPu.

Consistent with a previous report (Albin et al., 1989), we observed GFP+ axon fibers in the EP and SNr (Figures 2E and 2F) and RFP+ fibers in the GPe (Figure 2I). Furthermore, we observed that axon collaterals of dMSNs were distributed in the GPe as well (Figures 2C and 2D). The GPe contained a substantial number of GFP+ axonal fibers (Figure 2C), which were not merely passing fibers of dMSNs, as axon varicosities were clearly observed in GFP+ axon fibers in the GPe, as well as in RFP+ fibers (Figures 2D and 2J). Recently, it
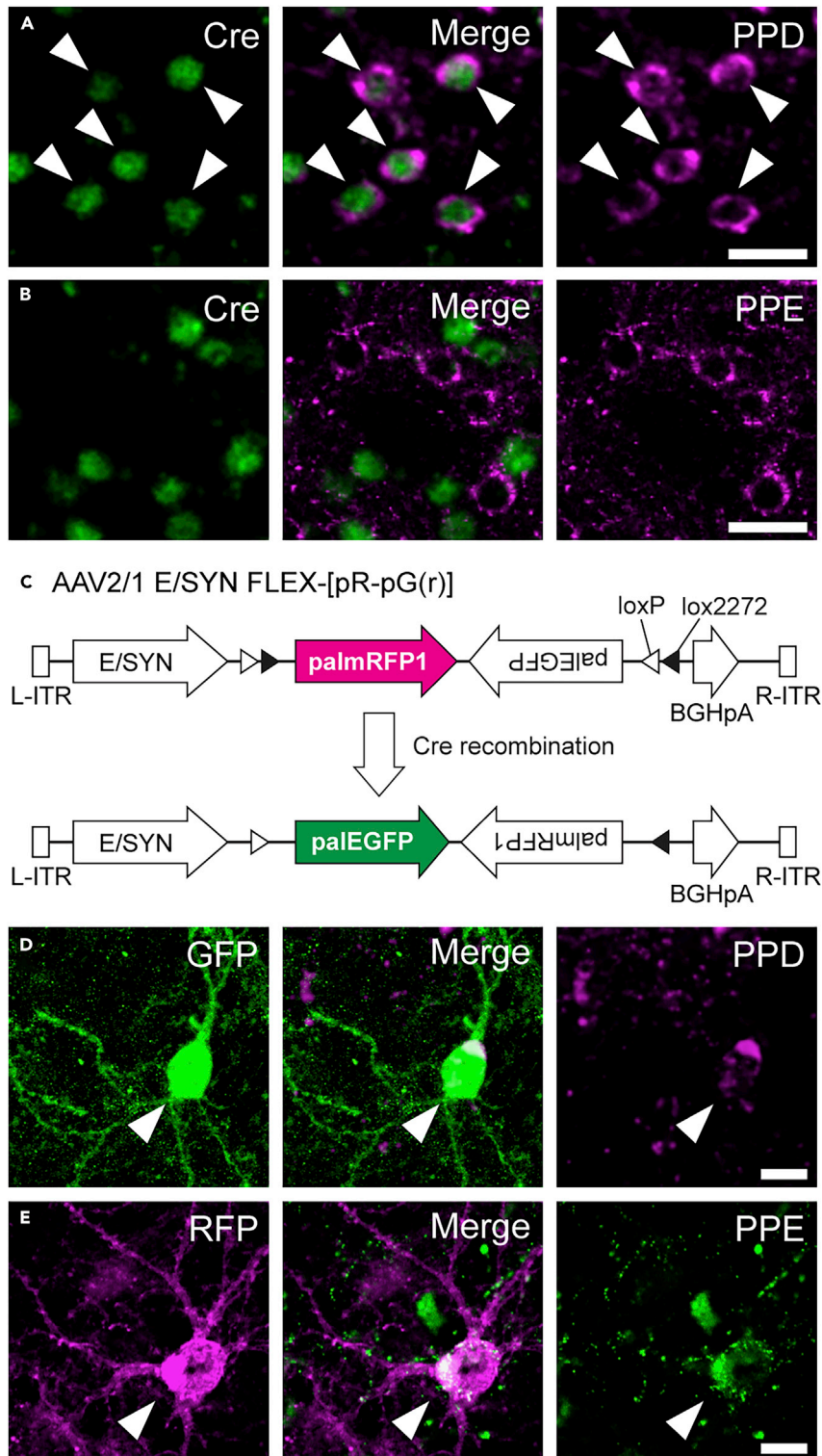
Figure 1. Specific Expression of GFP and RFP in Direct or Indirect Pathway Neurons

(A and B) Double immunostaining for Cre recombinase and PPD or PPE in the CPu of Drd1-Cre transgenic mice. Immunoreactivity for Cre recombinase was observed in almost all PPD-immunoreactive cells (arrowheads) but not in PPE-positive cells. Scale bars: 20 μm.

Figure 1. *Continued*

(C) AAV2/1-E/SYN-FLEX-[pR-pG(r)] vector. In the absence of Cre recombinase, the vector expresses palmitoylation site-attached mRFP1, palmRFP1 (pR). In contrast, the vector produces palmitoylation site-attached EGFP, palEGFP (pG), only in the presence of Cre recombinase by inverting the FLEX cassette.

(D and E) Expression of reporter proteins in neostriatal neurons. One week after AAV vector injections, most GFP+ and RFP+ cells were immunoreactive for PPD and PPE, respectively. Arrowheads indicate double-positive neurons. Scale bars: 10 μm.

has been reported that there is direct projection from the rat neocortex to the GPe (Karube et al., 2019). We confirmed that brain regions other than the CPu, such as the neocortex and thalamus, were not infected in the present study (Figure S1). A few RFP+ axon fibers were observed in the EP and SNr (Figures 2K and 2L). This is in accordance with a previous report, in which only 1.0% of PPE+ neurons projected to the SN (Lee et al., 1997).

Distinct Axonal Arborizations Formed by dMSNs and iMSNs in the GPe

We investigated the distributions of GFP+ and RFP+ axon fibers in the GPe by AAV vector injections into the CPu of Drd1-Cre mice. We first quantified the number of GFP+ and RFP+ MSNs in each mouse and superimposed the locations of cell bodies in the parasagittal plane (Figure 3). The numbers of GFP+ and RFP+ MSNs were 28.7 ± 17.3 and 22.8 ± 14.0, respectively (mean ± SD, n = 6 mice). The cell bodies of GFP+ and RFP+ MSNs were distributed in the range of 0.52 ± 0.13 and 0.44 ± 0.11 mm in the rostro-caudal plane, 0.80 ± 0.15 and 0.72 ± 0.19 mm in the dorsoventral plane, and 0.53 ± 0.08 and 0.48 ± 0.10 mm in the mediolateral plane, respectively (mean ± SD, n = 6 mice). There was no obvious difference in the distributions of GFP+ and RFP+ cell bodies in the CPu.

After tracing GFP+ and RFP+ axon fibers in separate sections, two adjacent sections were superimposed in the parasagittal plane (Figures 4 and S2). RFP+ axon fibers were distributed over a wider range and at a higher density than that of GFP+ axon fibers. The projection fields of GFP+ and RFP+ axon fibers in the GPe were 0.63 ± 0.10 and 0.65 ± 0.13 mm in the rostrocaudal plane, 0.81 ± 0.12 and 0.92 ± 0.12 mm in the dorsoventral plane, and 0.62 ± 0.22 and 0.87 ± 0.16 mm in the mediolateral plane, respectively (mean ± SD, n = 6 mice). Thus, iMSNs exhibited wider and denser innervation of the GPe than that of dMSNs.

We subsequently analyzed the axonal distributions of dMSNs and iMSNs in the GPe. Both RFP+ and GFP+ fibers formed two axonal arborizations in the parasagittal plane, although the two arborizations were not clear in the trace image of mouse #3 (Figure S2). To determine the centers of the projection fibers, the densities of GFP+ and RFP+ varicose fibers in the GPe were quantified. We divided the GPe into 40 μm × 40 μm boxes in each parasagittal section and calculated the length of varicose axon fibers in each box, from which we generated a heatmap of axon density (Figures 5A, S3, and S4). The map reflected wider and denser distributions of RFP+ varicose fibers than GFP+ fibers, as shown in the trace images. The densities of GFP+ and RFP+ varicose fibers were individually fitted with two three-dimensional (3D) Gaussian distributions. We estimated regions where the Mahalanobis distance from the center was less than 1, which contains approximately 20% of the points drawn from the fitted Gaussian distribution. The distributions of GFP+ and RFP+ varicose fibers mostly overlapped (Figures 5B, S3, and S4). Next, the center of each Gaussian distribution was determined, and the rostral and caudal positions were named as Arborizations #1 and #2, respectively. These two 3D Gaussian fittings could likely represent two arborizations of MSNs in the GPe, even for mouse #3 (Figure S3). The distances between arborizations, which were defined as the Euclidean distances between the centers of the Gaussian distributions fitted to the arborizations, were calculated (Figure 5C). The distance between two GFP+ or RFP+ arborizations (G1-G2 or R1-R2) was significantly greater than the distance between overlapping GFP+ and RFP+ arborizations (G1-R1 or G2-R2) (Figure 5D; n = 6 mice). Collectively, these findings indicated that dMSNs and iMSNs formed two axonal arborizations in the GPe and that the center locations that dMSN and iMSN axon fibers targeted were almost overlapped in the GPe.

Overlapping Projection Areas of dMSNs and iMSNs in the GPe

In addition to the target centers of MSNs in the GPe, we analyzed the projection area of GFP+ and/or RFP+ axon fibers in the GPe, focusing on the area where the axons were distributed rather than on axon density. We divided the GPe into 40 μm × 40 μm boxes and classified individual boxes based on the presence of
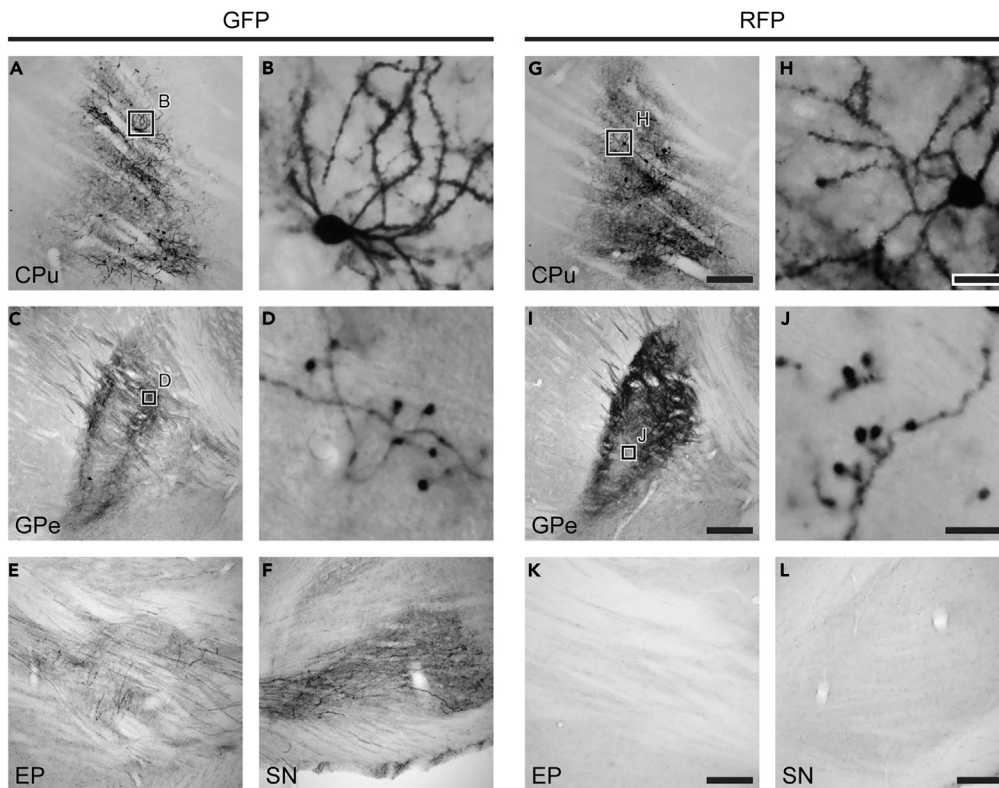
Figure 2. Labeling of Direct or Indirect Pathway Neurons by the AAV Vector

(A and G) Injection sites of the AAV vector. The infected area was restricted to the CPu. Scale bars: 200 μm.

(B and H) Higher magnification images of infected neurons in (A) and (G). Dendritic spines were clearly observed in both GFP+ and RFP+ neurons; these neurons were thus considered to be medium-sized spiny neurons (MSNs). Scale bars: 20 μm.

(C, D, I, and J) GFP and RFP immunoreactivities in the GPe. Both GFP+ and RFP+ fibers were observed in the GPe. Boutons were clearly observed in GFP+ and RFP+ fibers. Scale bars: 200 μm (C and I) and 10 μm (D and J).

(E, F, K, and L) GFP and RFP immunoreactivities in the EP and SN. GFP+ fibers were observed in the EP and SN, whereas RFP+ fibers were rarely detected in these output nuclei. Scale bars: 200 μm. See also Figure S1.

GFP+ and/or RFP+ varicose fibers (Figure 6A). In the lateral and medial sections of each mouse, RFP+ varicose fibers were predominant, whereas GFP+ fibers were rarely observed (Figures 6B and S5). Conversely, in the middle sections located between the lateral and medial sections of each mouse, the projection area of GFP+ fibers increased, mostly overlapping with the area containing RFP+ fibers. The number of boxes were counted in each parasagittal section, and the percentage of GFP+ and/or RFP+ projection areas in all sections was determined (Figure 6C). In all mice, half of the axon projection areas were positive only for RFP, showing that iMSNs projected to the GPe over a wider range than dMSNs. Most GFP+ fiber projection areas were included in the RFP+ projection areas. The ratios of boxes positive for RFP only, GFP only, and both were 58.2 ± 10.7%, 10.2 ± 5.7%, and 31.5 ± 5.9%, respectively (mean ± SD, n = 6 mice). Thus, in the GPe, dMSN axon collaterals converged proximally in the center of the field that receives axonal projections from neighboring iMSNs.

Topographical Projections of dMSNs and iMSNs to the GPe

The fact that neighboring dMSNs and iMSNs sent axons to the nearby subfield in the GPe suggests topographical organization of striatopallidal pathway. We then investigated the relationship between the positions of the infected MSNs in the CPu and the distributions of axon fibers in the GPe. The centers of the infected soma distributions were calculated from Figure 3, and the centers of the axon projections were determined using Arborizations #1 and #2 estimated in Figure 5C (n = 6 mice). The 3D coordinates from bregma were determined with reference to the brain atlas (Franklin and Paxinos, 2007), and the
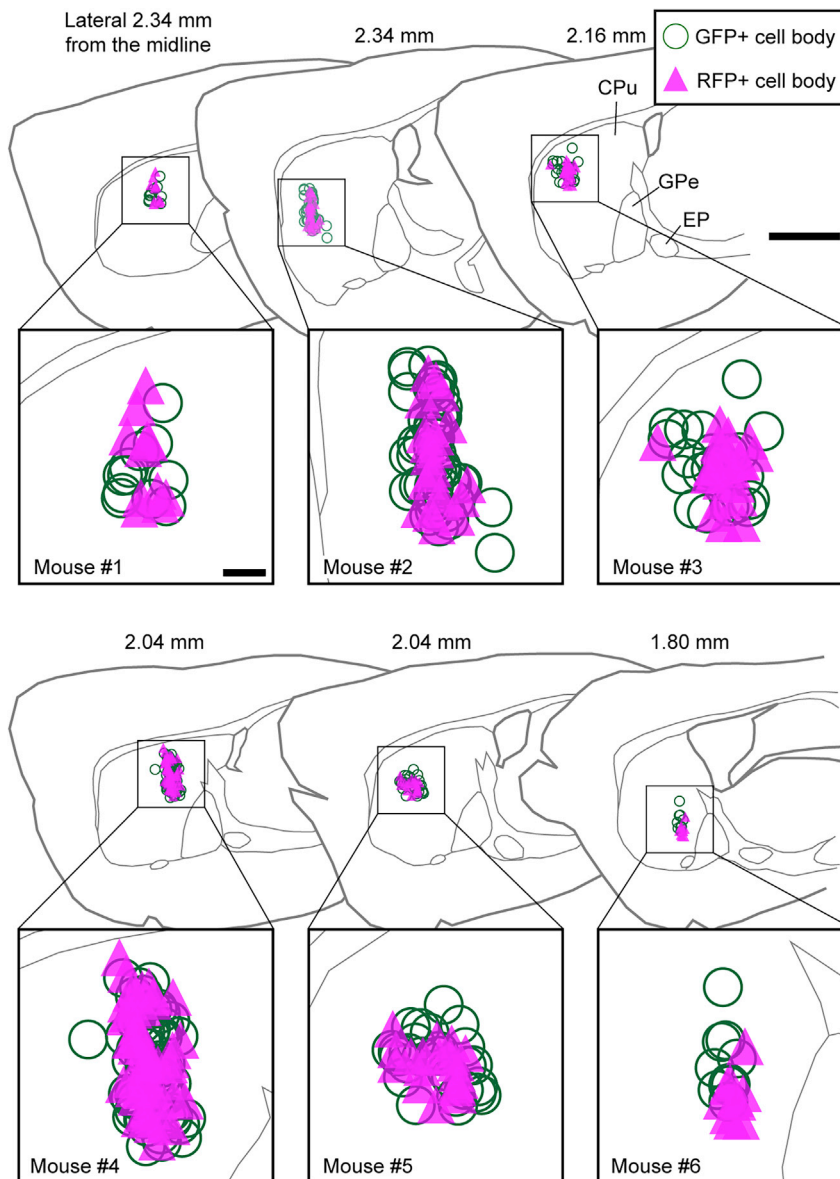
Figure 3. Distribution of GFP+ or RFP+ MSN Somata

The locations of GFP+ or RFP+ cell bodies were superimposed onto parasagittal sections exhibiting the highest infection density in each mouse. Green circles and magenta triangles indicate GFP+ and RFP+ cell bodies, respectively. Scale bars: 1 mm and 200 μm (insets).

centers of axonal arborizations were compared with those of soma distributions (Figure 7). In the rostrocaudal plane, no clear correlation was found in the present study (Figures 7A and 7D). In the dorsoventral plane, there was a strong correlation between the infection and projection sites in Arborization #2 (Figure 7E). In Arborization #1, the dorsoventral distribution of GFP+ axon fibers also tended to correlate with that of GFP+ cell bodies, even though this correlation was not statistically significant (Figure 7B). In the mediolateral plane, very strong correlations were detected in both Arborizations #1 and #2 (Figures 7C and 7F). This result demonstrates that the mediolateral and dorsoventral topography of neostriatal cell bodies are credible in both dMSN and iMSN axons targeting the GPe.

Moreover, the striatopallidal circuit topography is known to be based on calbindin (CB) immunoreactivity, where MSNs in the CB-rich region in the CPu project to the CB-rich region in the GPe, and vice versa (Kita
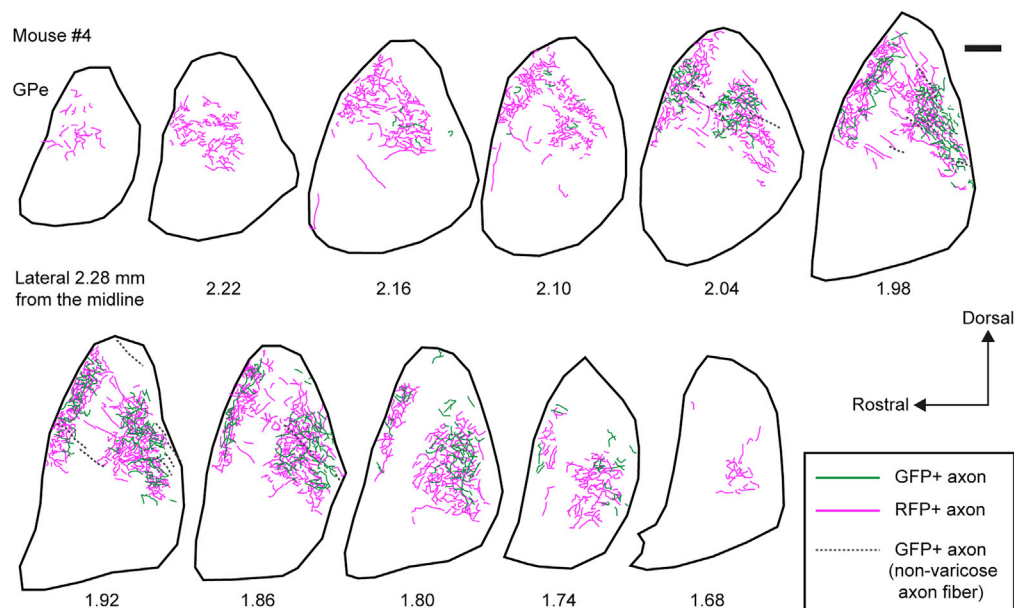
Figure 4. Projections of GFP+ or RFP+ Fibers to the GPe

Green and magenta lines indicate GFP+ and RFP+ varicose fibers, respectively, in mouse #4. GFP+ fibers without varicosities are indicated by gray lines. All RFP+ fibers were varicose. Both GFP+ and RFP+ varicose fibers formed two axonal arborizations in the parasagittal plane. Widespread RFP+ fibers were observed in the GPe, whereas the distribution of GFP+ fibers was almost completely confined within that of RFP+ fibers. Scale bar: 200 μm. See also Figure S2.

and Kita, 2001); the GPe has also been reported to be divided into two regions depending on CB immunoreactivity (Kita and Kita, 2001), which appeared to be similar to the distribution of MSN axonal arborizations revealed in the present study. Therefore, we finally examined the overlap between CB immunoreactivity and GFP+ and RFP+ axon fibers in the GPe. One week after AAV vector injections, we performed triple immunofluorescence staining for CB, GFP, and RFP. CB immunoreactivity was strong in the rostral region near the boundary between the CPu and GPe and in the caudal part of the GPe (CB-rich region), whereas the immunoreactivity was weak in the intermediate zone (CB-poor region) (Figure 8A). The immunoreactivities for GFP and RFP were strong in the CB-rich regions and weak in the CB-poor regions, consistent with changes in the intensity of CB immunoreactivity (Figures 8A–8D). When the fluorescence intensities of GFP+ and RFP+ axons were quantified, the axons of both cell types were significantly more abundant in the CB-rich region than in the CB-poor region (p < 0.001 for GFP+, p < 0.001 for RFP; n = 3 mice) (Figure 8E). Similar to the results of immunoperoxidase staining, fluorescence imaging revealed that dMSNs and iMSNs projected to the same regions of the GPe and that iMSNs had a wider projection range (Figures 8B–8D).

DISCUSSION

In this study, we characterized the axonal projection patterns of dMSNs as well as iMSNs in the GPe by using the AAV vector that selectively labels neighboring dMSNs and iMSNs with different fluorescent proteins. Both dMSNs and iMSNs formed two axonal arborizations in the rostral and caudal parts of the GPe and showed topographical projections in the dorsoventral and mediolateral planes. The axon fibers of dMSNs displayed a spatially limited distribution within the iMSN-targeted subfield in the GPe (Figure 9). This overlapping topography of the respective projections would contribute to linking information from direct and indirect pathway neurons within the GPe.

Although we analyzed the projections of dMSNs and iMSNs to the GPe using anterograde labeling with the AAV vector, we did not confirm the projections by retrograde tracing techniques in the present study. As iMSNs project to a wider range of the GPe and only a portion of dMSNs send axon collaterals to the GPe (Fujiyama et al., 2011), more iMSNs than dMSNs would be labeled by retrograde labeling. Indeed, it has been reported that injection of rhodamine dextran amine 3 kDa into the GPe labeled neostriatal neurons positive for Drd2 about four times more than neurons immunoreactive for Drd1 (Deng et al., 2006).
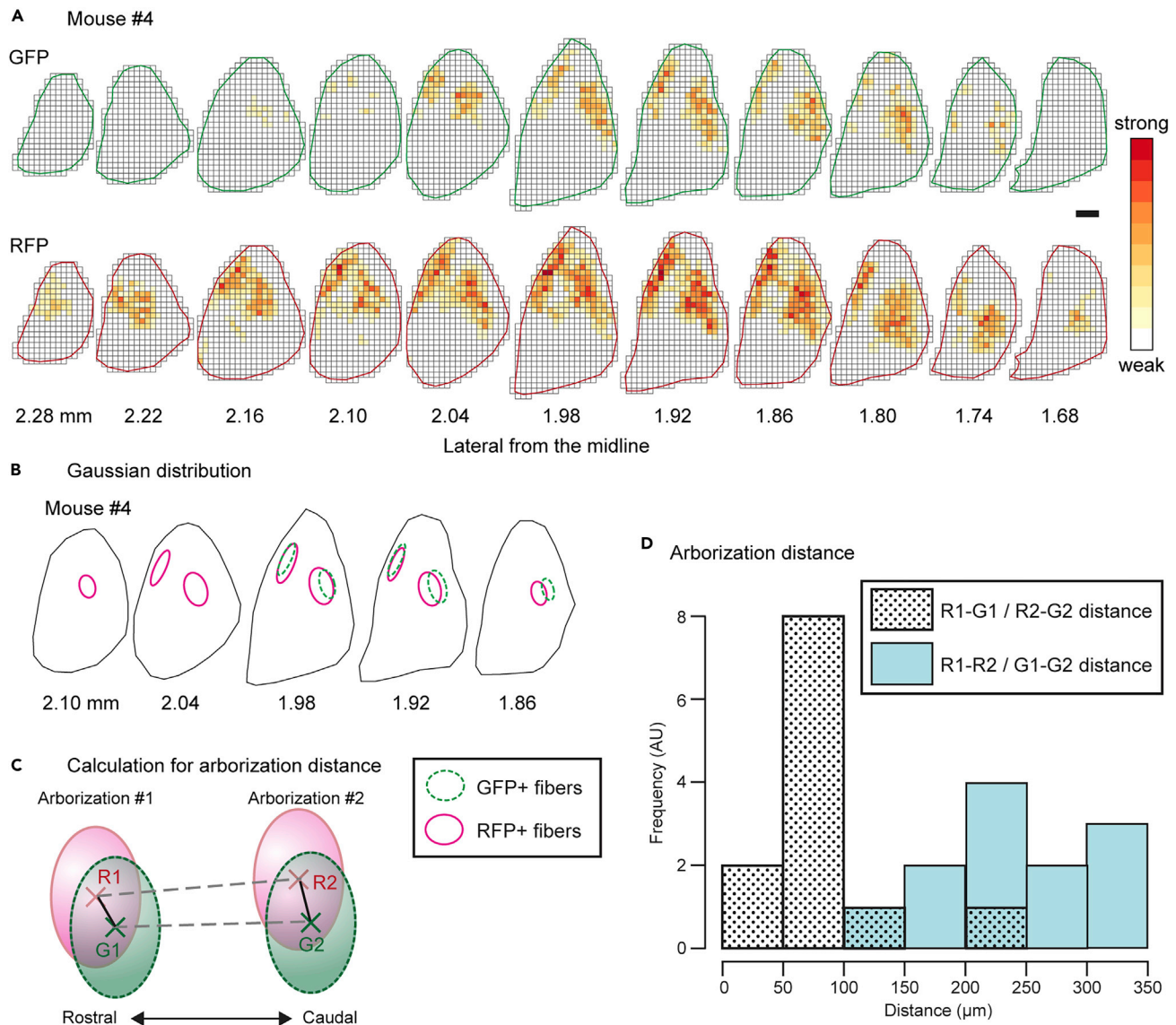
Figure 5. Density Analysis of GFP+ and/or RFP+ Axon Fibers in the GPe

(A) Heatmap of fiber density in mouse #4. Pseudocolor represents the length of the varicose fibers in each box (40 μm × 40 μm). RFP+ fibers displayed a wider distribution and higher density than that of GFP+ fibers throughout the GPe. Scale bar: 200 μm.

(B) Modeling of the density of axonal fibers by a mixture of two 3D Gaussian distributions in mouse #4. The green and magenta ellipses correspond to points with a Mahalanobis distance of 1 from the center of the Gaussian distributions fitted to GFP+ and RFP+ fibers, respectively.

(C) Calculation of the Euclidean distances between the centers of the Gaussian distributions fitted to the arborizations. The crosses (G1, G2, R1, and G2) are the centers of the Gaussian distributions fitted to GFP+ (green) and RFP+ (magenta) fibers. Arborizations #1 (G1 and R1) and #2 (G2 and R2) represent the centers of the rostral and caudal arborizations.

(D) Histogram of the distance between the axonal arborizations. R1-R2 and G1-G2 distances were significantly larger than R1-G1 and R2-G2 distances, indicating that both GFP+ and RFP+ fibers formed two axonal arborizations in the GPe, and the centers of GFP+ and RFP+ axonal arborizations mostly overlapped (p = 0.00002875, Kolmogorov-Smirnov test; n = 6 mice). See also Figures S3 and S4.

In Drd1-Cre transgenic mice, Cre recombinase is specifically expressed in dMSNs, enabling labeling of dMSNs with GFP by the flip-excision (FLEX) (Schnutgen et al., 2003) switch-containing AAV vector in the present study. As RFP is expressed in the absence of Cre recombinase, both iMSNs and interneurons were labeled with RFP. MSNs account for 90%–98% of all neurons in the CPu (Kawaguchi et al., 1995; Kemp and Powell, 1971; Rymar et al., 2004). The remaining neurons are cholinergic or GABAergic interneurons (Kreitzer, 2009). Since the cell bodies of cholinergic interneurons are large (Kawaguchi, 1993), they are
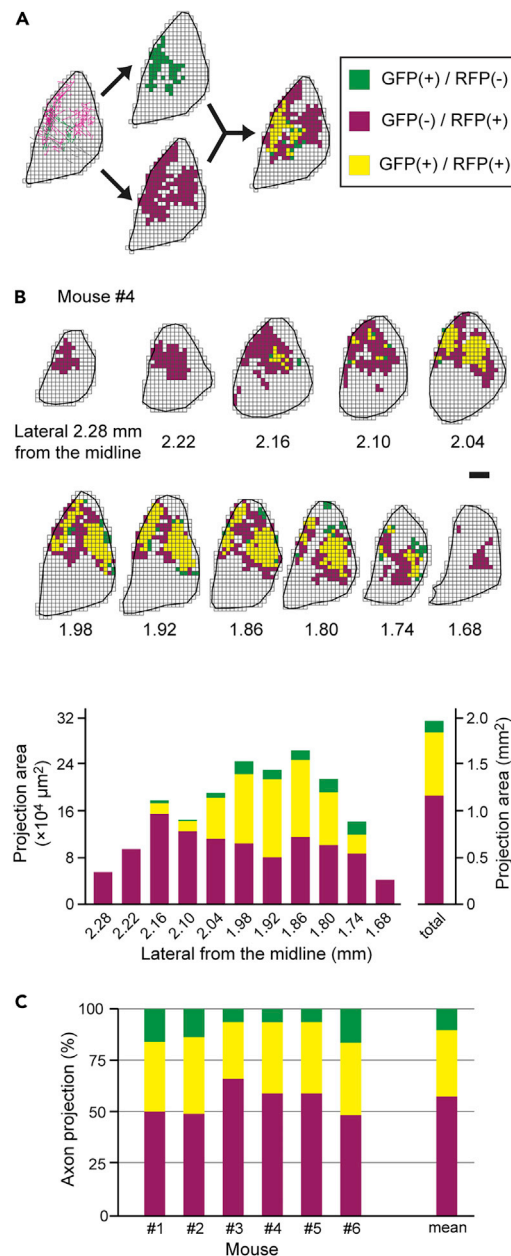
Figure 6. Area Analysis of GFP+ and/or RFP+ Axon Fiber Distribution in the GPe

(A) Method of analysis of the axon projection area. The GPe was subdivided into 40 μm × 40 μm boxes, and axonal distribution was binarized depending on whether they contained GFP+ or RFP+ fibers, shown in green or red, respectively. The yellow boxes represent areas containing fibers that were positive for both GFP and RFP. Scale bar: 200 μm.

(B) An example of the area analysis in mouse #4. The number of each box type was counted in parasagittal sections and converted to the area [$\times 10^4$ μm^2]. Each of these areas [$\times 10^4$ μm^2] and their sums [mm^2] are represented by a bar graph. Note that the "total" here is the sum of the areas calculated for the analyzed sections and does not represent the total number of actual axon projection fields.

(C) Each bar chart shows the percentage of the total number of each box type in six mice. The rightmost bar indicates the average of all mice. GFP+ fibers converged in RFP+ projection areas. Green, red, and yellow bars indicate boxes containing GFP+, RFP+, and both GFP+/RFP+ fibers. See also Figure S5.

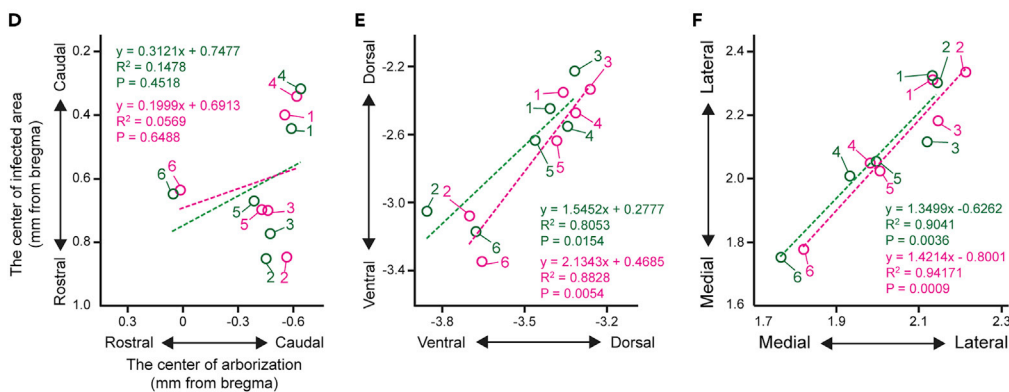## Arborization #1
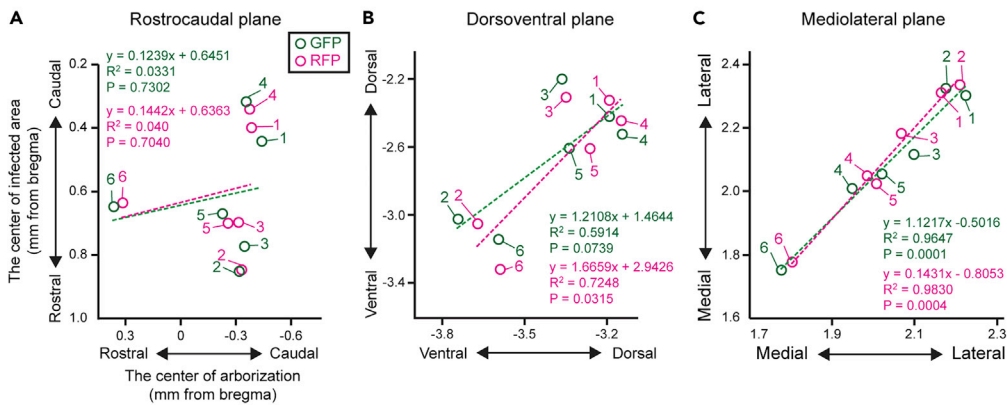
Arborization #2

Figure 7. Topographical Projections of dMSNs and iMSNs to the GPe

For Arborizations #1 and #2, the centers of the infected MSN somata and axonal arborizations are plotted along the rostrocaudal (A and D), dorsoventral (B and E), and mediolateral planes (C and F) (n = 6 mice). The vertical and horizontal axes represent the centers of the infected areas in the CPu and the axonal arborizations in the GPe, respectively. Green and magenta circles indicate the positions of GFP and RFP in each mouse. Dotted lines indicate linear regression lines. Strong correlations were found in the dorsoventral and mediolateral planes.

easily distinguished from MSNs and other GABAergic interneurons by large differences in cell body size. Although the somata of GABAergic interneurons are similar in size to those of MSNs, they are characterized by non-spiny dendrites (Bennett and Bolam, 1993; Kawaguchi, 1993) and can be discriminated from MSNs by the absence of spines. When analyzing the number and distribution of the infected MSNs in the CPu, non-MSN cells were excluded based on these morphological features. In addition, since the axons of interneurons remain within the CPu, they did not confound the present analysis, which assessed the density and area of dMSN and iMSN axon fibers within the GPe. Therefore, we successfully evaluated the axon projections of dMSNs and iMSNs to the GPe.

Topographical projections of dMSNs and iMSNs to the GPe were clearly observed in the dorsoventral and mediolateral planes, a finding that was in good accordance with that of a previous study demonstrating similar topographical projections of a mixture of dMSNs and iMSNs (Gerfen, 1985). Using the method developed in the present study, we successfully labeled dMSNs and iMSNs separately and demonstrated that each of them projects topographically. The topographic organization of striatopallidal projections in the rostrocaudal plane has also been reported using an autoradiographic tracer (Wilson and Phelan, 1982). However, no clear correlation was detected between the infected MSN somatic positions and the axon fiber distributions in the present study. Regardless of the locations of the infected MSN somata in the CPu, the axon projections appeared to converge at approximately the same position in the GPe: Arborizations #1 and #2 were distributed in the range of −0.3 to −0.5 mm and −0.4 to −0.6 mm, respectively, except in
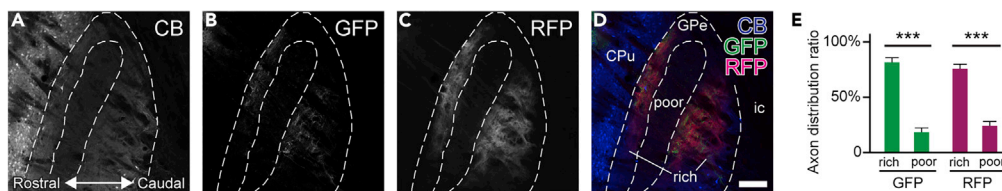
Figure 8. Overlap Distribution of CB Immunoreactivity and MSN Axon Fibers in the GPe

(A–D) Distributions of CB, GFP, and RFP immunoreactivities in the GPe. One week after AAV vector injections into the CPu of Drd1-Cre mice, brain sections were immunostained for CB, GFP, and RFP. The GPe can be divided into two regions— CB-rich and CB-poor—according to the immunoreactivity for CB. Scale bar: 100 μm.

(E) The total immunofluorescence intensities of GFP and RFP in CB-rich and CB-poor regions were normalized to 1 arbitrary unit in each mouse, and the respective percentages were calculated. Data are represented as mean ± SD. A significant difference was detected between the two regions in both GFP and RFP (Tukey's post hoc test; ***p < 0.001; n = 3 mice).

mouse #6. It is possible that mouse #6, whose infected area was located most ventromedially, exhibited a different projection pattern. Further studies are required for comprehensive clarification of striatopallidal topography, especially in the rostrocaudal plane, using 3D quantitative analysis in large samples.

The GPe is known to be divided into two regions—CB-rich and CB-poor regions (Kita and Kita, 2001). We have demonstrated that both dMSNs and iMSNs send axons to the CB-rich region in the GPe. Furthermore, it has been reported that the CPu also contains CB-rich and CB-poor regions and that each makes reciprocal connections with the corresponding regions of the GPe (Kita and Kita, 2001). In the present study, no projection of MSNs to the CB-poor region in the GPe were noted, probably because CB-poor regions in the CPu are confined to a narrow dorsolateral region and the AAV vector did not infect the CB-poor regions in the CPu. It would be interesting to apply more sophisticated methods to comprehensively analyze the reciprocal connections between the corresponding regions in the CPu and GPe.

The present study demonstrated that dMSNs and iMSNs formed two axonal arborizations in the same regions of the GPe. These overlapping projections may form the structural basis for cooperative function of dMSNs and iMSNs, consistent with the emerging model of the basal ganglia (Peak et al., 2019). It has been proposed that axon collaterals of dMSNs in the GPe link information from direct and indirect pathway neurons within the GPe (Cazorla et al., 2014). Indeed, the excitability of iMSNs bidirectionally regulates the amount of dMSN axon collaterals in the GPe: chronic enhancement or suppression of iMSN excitability increased or decreased the amount of dMSN projections to the GPe, respectively, suggesting that plasticity may regulate the output balance from the neostriatum (Cazorla et al., 2014). It will be necessary to examine the mechanisms of axonal plasticity of dMSNs and iMSNs in the GPe in more detail, considering the convergent projections revealed in the present study.

Our present findings of convergence of dMSN axons in the central area of iMSN projections in the GPe extend the classical model of the basal ganglia. In the classical model, dMSNs enhance the activity of thalamic neurons through output nuclei (EP and SNr) and facilitate desired actions, whereas iMSNs suppress competing movements by inhibiting the thalamus (Albin et al., 1989; Mink, 1996). The axons of iMSNs, which spread more widely in the GPe, achieve surround suppression of thalamic neuron activity. Conversely, dMSNs may enhance the activity of thalamic neurons and strongly suppress thalamic activity with a slight time delay by axon collaterals to the GPe accelerating the indirect pathway. This feedforward inhibition may enhance temporal resolution of thalamic neuron activity.

Limitations of the Study

In this study, the distribution of axon fibers in the GPe was analyzed using bright-field staining for GFP or RFP in 20-μm-thick adjacent sections, but all fibers were not visualized and quantified. In order to accurately estimate the length and distributions of GFP+ and RFP+ fibers in the GPe, the fibers should be fully reconstructed in 3D. Owing to the high density of the projecting fibers to the GPe, it is laborious to perform a full 3D reconstruction with thin sections, and it would be more efficient to observe the fibers three-dimensionally with thicker specimens, such as slices and hemispheres, using a tissue-clearing method.
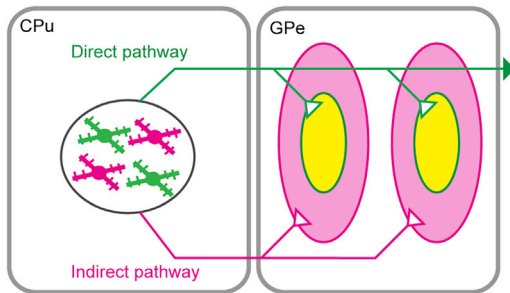
Figure 9. Schematic Diagram of Direct and Indirect Pathways in the GPe
dMSNs and iMSNs are shown in green and magenta, respectively. Regions containing fibers positive for both GFP and RFP are displayed in yellow.

Furthermore, we analyzed the projections of dMSNs and iMSNs using only Drd1-Cre mice but not Drd2- or A2a-Cre mice, which express Cre recombinase specifically in iMSNs in the CPu. The use of these strains would have led to more convincing conclusions about the overlapping projections of dMSNs and iMSNs to the GPe.

Finally, and most importantly, the current technique does not allow us to determine whether dMSNs and iMSNs target the same or different neurons in the GPe. Therefore, in order to elucidate the functional significance of the overlapping projections revealed in this study, it is important to identify the types of GPe neurons that receive synaptic inputs from dMSNs and/or iMSNs in future studies.

Resource Availability

Lead Contact
Further information and requests for resources and reagents should be directed to and will be fulfilled by the Lead Contact, Hiroyuki Hioki (h-hioki@juntendo.ac.jp).

Materials Availability
All unique biological materials generated in this study are available from the lead contact with a completed materials transfer agreement.

Data and Code Availability
All data and custom scripts used in this study are available upon request.

METHODS

All methods can be found in the accompanying Transparent Methods supplemental file.

SUPPLEMENTAL INFORMATION

Supplemental Information can be found online at https://doi.org/10.1016/j.isci.2020.101409.

ACKNOWLEDGMENTS

AUTHOR CONTRIBUTIONS

DECLARATION OF INTERESTS

REFERENCES

Albin, R.L., Young, A.B., and Penney, J.B. (1989). The functional anatomy of basal ganglia disorders. Trends Neurosci. *12*, 366–375.

Alexander, G.E., and Crutcher, M.D. (1990). Functional architecture of basal ganglia circuits: neural substrates of parallel processing. Trends Neurosci. *13*, 266–271.

Bennett, B.D., and Bolam, J.P. (1993). Characterization of calretinin-immunoreactive structures in the striatum of the rat. Brain Res. *609*, 137–148.

Cazorla, M., de Carvalho, F.D., Chohan, M.O., Shegda, M., Chuhma, N., Rayport, S., Ahmari, S.E., Moore, H., and Kellendonk, C. (2014). Dopamine D2 receptors regulate the anatomical and functional balance of basal ganglia circuitry. Neuron *81*, 153–164.

Chang, H.T., Wilson, C.J., and Kitai, S.T. (1981). Single neostriatal efferent axons in the globus pallidus: a light and electron microscopic study. Science *213*, 915–918.

Cui, G., Jun, S.B., Jin, X., Pham, M.D., Vogel, S.S., Lovinger, D.M., and Costa, R.M. (2013). Concurrent activation of striatal direct and indirect pathways during action initiation. Nature *494*, 238–242.

DeLong, M.R. (1990). Primate models of movement disorders of basal ganglia origin. Trends Neurosci. *13*, 281–285.

Deng, Y.P., Lei, W.L., and Reiner, A. (2006). Differential perikaryal localization in rats of D1 and D2 dopamine receptors on striatal projection neuron types identified by retrograde labeling. J. Chem. Neuroanat. *32*, 101–116.

Franklin, K.B.J., and Paxinos, G. (2007). Paxinos and Franklin's the Mouse Brain in Stereotaxic Coordinates (Academic Press).

Fujiyama, F., Sohn, J., Nakano, T., Furuta, T., Nakamura, K.C., Matsuda, W., and Kaneko, T. (2011). Exclusive and common targets of neostriatofugal projections of rat striosome neurons: a single neuron-tracing study using a viral vector. Eur. J. Neurosci. *33*, 668–677.

Furuta, T., Tomioka, R., Taki, K., Nakamura, K., Tamamaki, N., and Kaneko, T. (2001). In vivo transduction of central neurons using recombinant Sindbis virus: Golgi-like labeling of dendrites and axons with membrane-targeted fluorescent proteins. J. Histochem. Cytochem. *49*, 1497–1508.

Gerfen, C.R. (1985). The neostriatal mosaic. I. Compartmental organization of projections from the striatum to the substantia nigra in the rat. J. Comp. Neurol. *236*, 454–476.

Gerfen, C.R., Engber, T.M., Mahan, L.C., Susel, Z., Chase, T.N., Monsma, F.J., Jr., and Sibley, D.R. (1990). D1 and D2 dopamine receptor-regulated gene expression of striatonigral and striatopallidal neurons. Science *250*, 1429–1432.

Gerfen, C.R., and Young, W.S., 3rd (1988). Distribution of striatonigral and striatopallidal peptidergic neurons in both patch and matrix compartments: an in situ hybridization histochemistry and fluorescent retrograde tracing study. Brain Res. *460*, 161–167.

Gong, S., Doughty, M., Harbaugh, C.R., Cummins, A., Hatten, M.E., Heintz, N., and Gerfen, C.R. (2007). Targeting Cre recombinase to specific neuron populations with bacterial artificial chromosome constructs. J. Neurosci. *27*, 9817–9823.

Graveland, G.A., and DiFiglia, M. (1985). The frequency and distribution of medium-sized neurons with indented nuclei in the primate and rodent neostriatum. Brain Res. *327*, 307–311.

Kameda, H., Furuta, T., Matsuda, W., Ohira, K., Nakamura, K., Hioki, H., and Kaneko, T. (2008). Targeting green fluorescent protein to dendritic membrane in central neurons. Neurosci. Res. *61*, 79–91.

Karube, F., Takahashi, S., Kobayashi, K., and Fujiyama, F. (2019). Motor cortex can directly drive the globus pallidus neurons in a projection neuron type-dependent manner in the rat. Elife *8*, e49511.

Kawaguchi, Y. (1993). Physiological, morphological, and histochemical characterization of three classes of interneurons in rat neostriatum. J. Neurosci. *13*, 4908–4923.

Kawaguchi, Y., Wilson, C.J., Augood, S.J., and Emson, P.C. (1995). Striatal interneurones: chemical, physiological and morphological characterization. Trends Neurosci. *18*, 527–535.

Kawaguchi, Y., Wilson, C.J., and Emson, P.C. (1990). Projection subtypes of rat neostriatal matrix cells revealed by intracellular injection of biocytin. J. Neurosci. *10*, 3421–3438.

Kemp, J.M., and Powell, T.P. (1971). The structure of the caudate nucleus of the cat: light and electron microscopy. Philos. Trans. R. Soc. Lond. B Biol. Sci. *262*, 383–401.

Kita, H., and Kita, T. (2001). Number, origins, and chemical types of rat pallidostriatal projection neurons. J. Comp. Neurol. *437*, 438–448.

Kreitzer, A.C. (2009). Physiology and pharmacology of striatal neurons. Annu. Rev. Neurosci. *32*, 127–147.

Le Moine, C., and Bloch, B. (1995). D1 and D2 dopamine receptor gene expression in the rat striatum: sensitive cRNA probes demonstrate prominent segregation of D1 and D2 mRNAs in distinct neuronal populations of the dorsal and ventral striatum. J. Comp. Neurol. *355*, 418–426.

Le Moine, C., Normand, E., Guitteny, A.F., Fouque, B., Teoule, R., and Bloch, B. (1990). Dopamine receptor gene expression by enkephalin neurons in rat forebrain. Proc. Natl. Acad. Sci. U S A *87*, 230–234.

Lee, T., Kaneko, T., Taki, K., and Mizuno, N. (1997). Preprodynorphin-, preproenkephalin-, and preprotachykinin-expressing neurons in the rat neostriatum: an analysis by immunocytochemistry and retrograde tracing. J. Comp. Neurol. *386*, 229–244.

Mink, J.W. (1996). The basal ganglia: focused selection and inhibition of competing motor programs. Prog. Neurobiol. *50*, 381–425.

Nishino, E., Yamada, R., Kuba, H., Hioki, H., Furuta, T., Kaneko, T., and Ohmori, H. (2008). Sound-intensity-dependent compensation for the small interaural time difference cue for sound source localization. J. Neurosci. *28*, 7153–7164.

Peak, J., Hart, G., and Balleine, B.W. (2019). From learning to action: the integration of dorsal striatal input and output pathways in instrumental conditioning. Eur. J. Neurosci. *49*, 658–671.

Preston, R.J., Bishop, G.A., and Kitai, S.T. (1980). Medium spiny neuron projection from the rat

striatum: an intracellular horseradish peroxidase study. Brain Res. *183*, 253–263.

Rymar, V.V., Sasseville, R., Luk, K.C., and Sadikot, A.F. (2004). Neurogenesis and stereological morphometry of calretinin-immunoreactive GABAergic interneurons of the neostriatum. J. Comp. Neurol. *469*, 325–339.

Schnutgen, F., Doerflinger, N., Calleja, C., Wendling, O., Chambon, P., and Ghyselinck, N.B. (2003). A directional strategy for monitoring Cre-mediated recombination at the

cellular level in the mouse. Nat. Biotechnol. *21*, 562–565.

Sonomura, T., Nakamura, K., Furuta, T., Hioki, H., Nishi, A., Yamanaka, A., Uemura, M., and Kaneko, T. (2007). Expression of D1 but not D2 dopamine receptors in striatal neurons producing neurokinin B in rats. Eur. J. Neurosci. *26*, 3093–3103.

Tecuapetla, F., Matias, S., Dugue, G.P., Mainen, Z.F., and Costa, R.M. (2014). Balanced activity in basal ganglia projection pathways is critical for

contraversive movements. Nat. Commun. *5*, 4315.

Wilson, C.J., and Phelan, K.D. (1982). Dual topographic representation of neostriatum in the globus pallidus of rats. Brain Res. *243*, 354–359.

Wu, Y., Richard, S., and Parent, A. (2000). The organization of the striatal output system: a single-cell juxtacellular labeling study in the rat. Neurosci. Res. *38*, 49–62.

Supplemental Information

Overlapping Projections of Neighboring

Direct and Indirect Pathway Neostriatal

Neurons to Globus Pallidus External Segment

Shinichiro Okamoto, Jaerin Sohn, Takuma Tanaka, Megumu Takahashi, Yoko Ishida, Kenta Yamauchi, Masato Koike, Fumino Fujiyama, and Hiroyuki Hioki

Table S1. Primers used in the present study, Related to Figure 1.

P1	5′-CTAGCAAAATAGGCTGTCCC<u>GAATTC</u>**GCCACC**ATGCTGTG CTGTAT-3′
P2	5′-GATCCACTAGTTCTAGAGCGTTAGGCGCCGGTGGAGTGGC-3′
P3	5′-CGCTCTAGAACTAGTGGATCTTACTTGTACAGCTCGTCCA-3′
P4	5′-GACGATAGTCATGCCCCGCG<u>GTCGAC</u>**GCCACC**ATGCTGTGCTGTAT-3′
P5	5′-AAAA<u>CTCGAG</u>TAGTTATTAATAGTAATCAA-3′
P6	5′-TTTT<u>GGATCC</u>CGCCGCAGCGCAGATGGTCG-3′

Bold characters indicate the Kozak consensus sequence. Underlined sequences indicate the restriction sites for *EcoR*I in P1, *Sal*I in P4, *Xho*I in P5, and *BamH*I in P6.
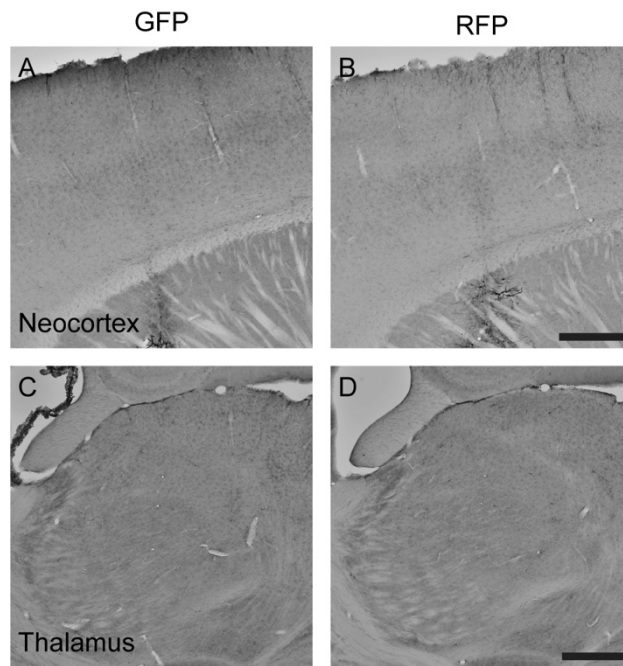
Figure S1. No infection of the AAV vector in the neocortex and thalamus, Related to Figure 2. (**A**, **B**) GFP and RFP immunoreactivities in the neocortex just above the injection site. The glass capillary passed through the neocortex during stereotaxic injection into the CPu, but there was no AAV infection in the neocortex (n = 6 mice). (**C**, **D**) GFP and RFP immunoreactivities in the thalamus. No immunoreactivity for GFP and RFP was observed in the thalamus (n = 6 mice). It was confirmed that there was no anterograde and/or retrograde infection in brain regions other than the CPu. Scale bars: 0.5 mm.
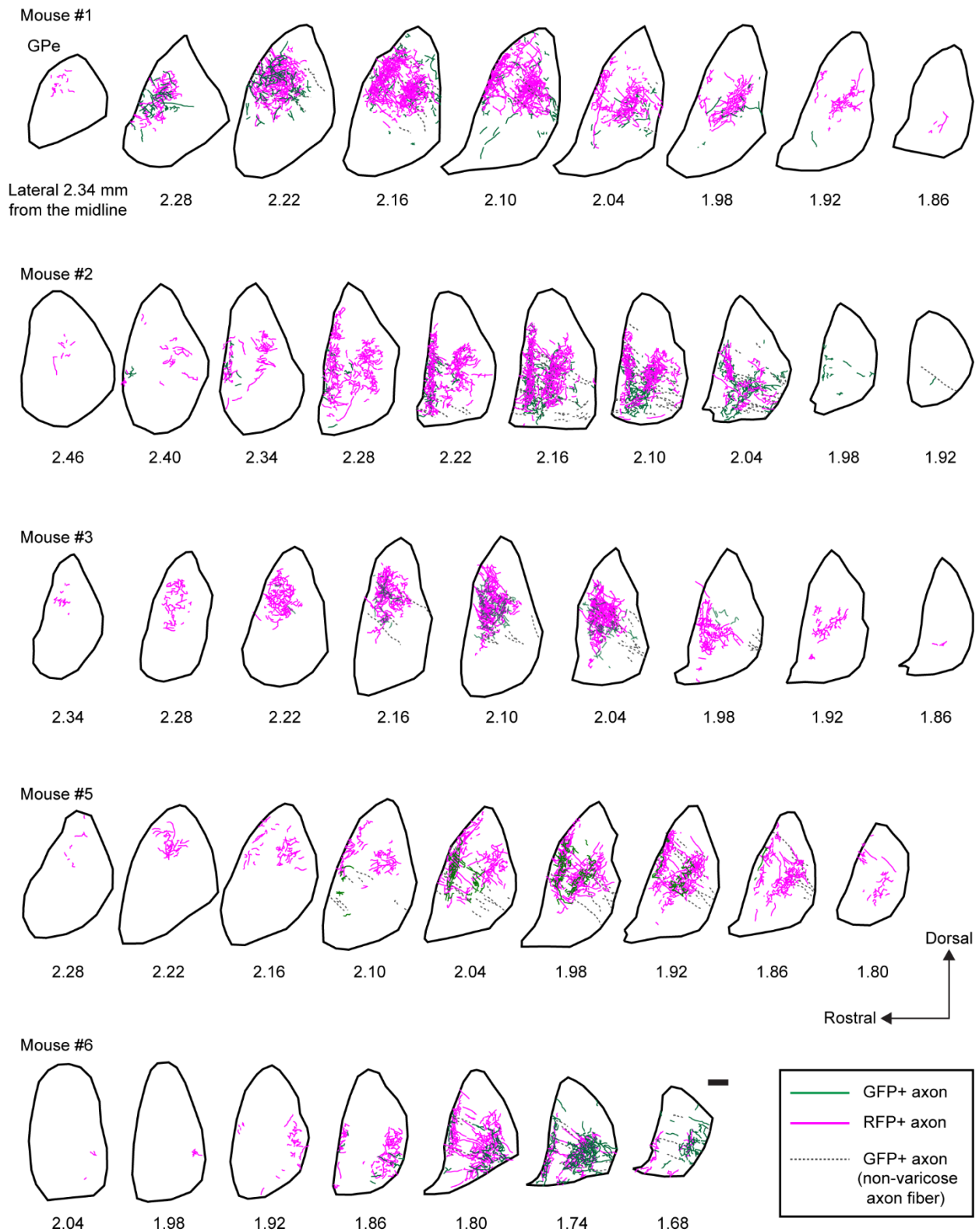
Figure S2. Projections of GFP+ or RFP+ fibers to the GPe, Related to Figure 4. Green and magenta lines indicate GFP+ and RFP+ varicose fibers, respectively, in mouse #1, #2, #3, #5, and #6. Fibers without varicosity were also found in GFP+ fibers (gray lines). Scale bar: 0.2 mm.

Figure S3. Density analysis of GFP+ and/or RFP+ axon fibers in the GPe in mouse #1, #2, and #3, Related to Figure 5. Fiber density heatmaps, where the pseudocolor represents the length of the varicose fibers in each boxed area (40 μm × 40 μm). Solid and dotted circles indicate Arborizations #1 and #2 located rostrally and caudally, respectively. Scale bar: 0.2 mm.

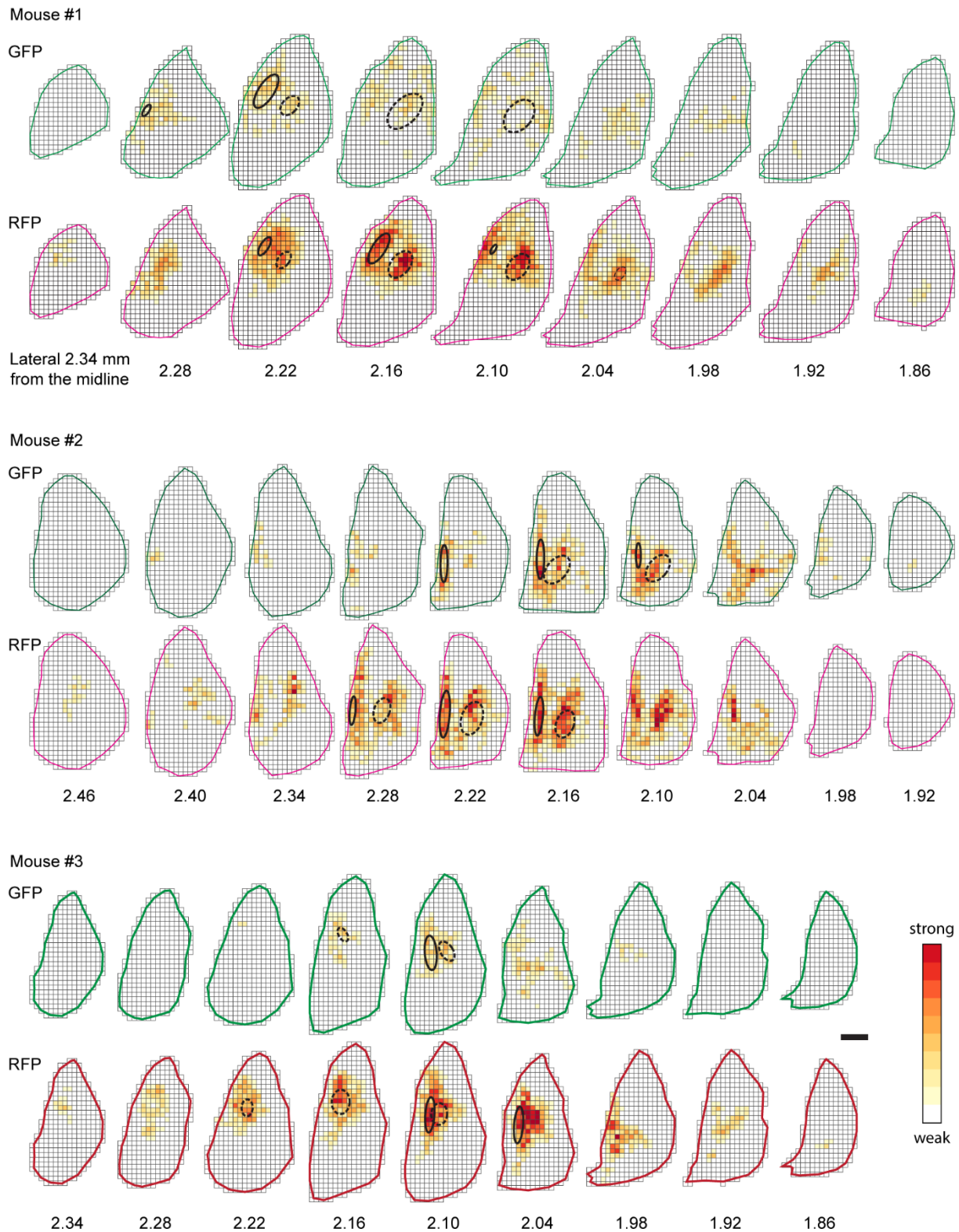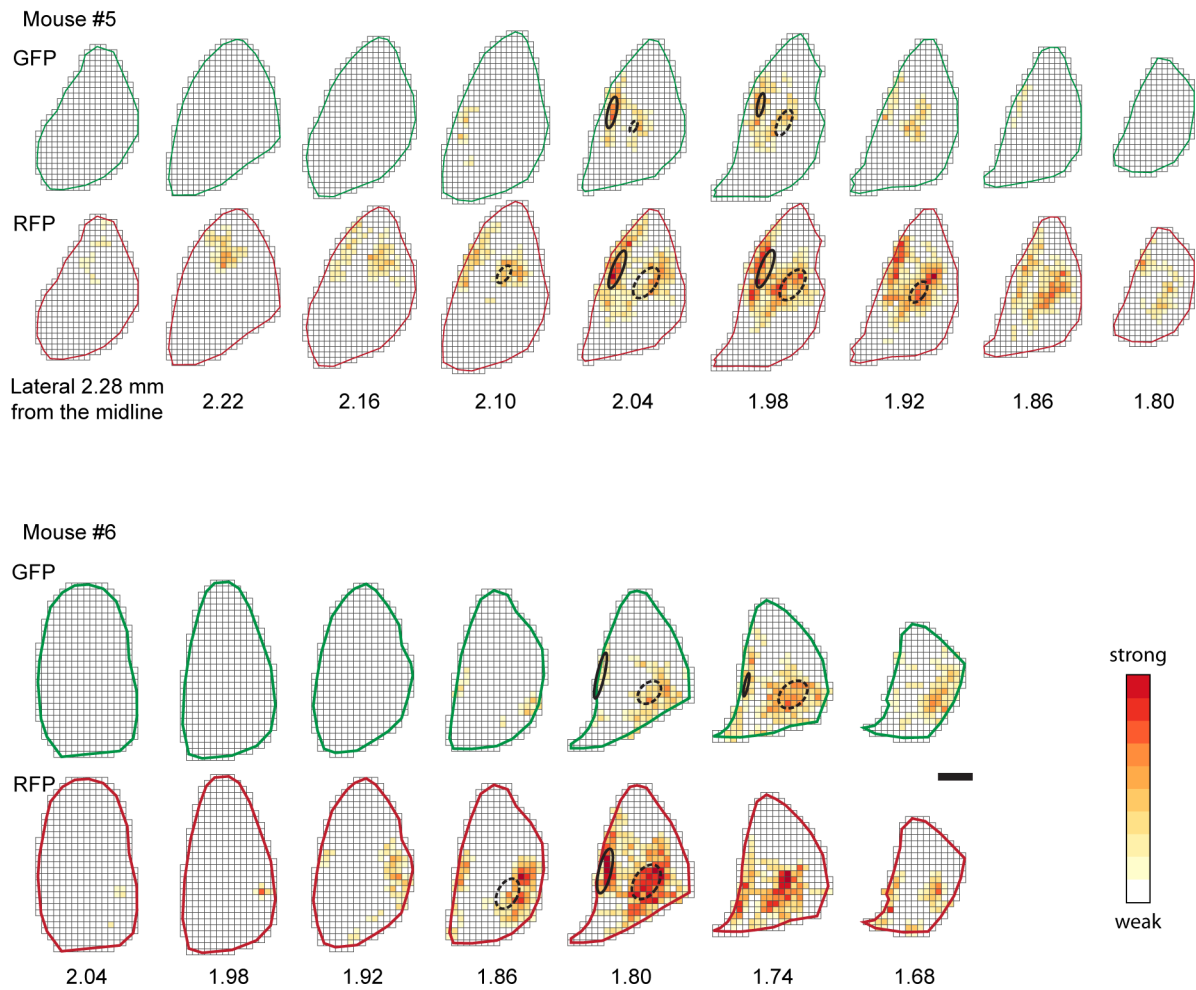**Figure S4. Density analysis of GFP+ and/or RFP+ axon fibers in the GPe in mouse #5 and #6, Related to Figure 5.** Fiber density heatmaps, where the pseudocolor represents the length of the varicose fibers in each boxed area (40 μm × 40 μm). Solid and dotted circles indicate Arborizations #1 and #2 located rostrally and caudally, respectively. Scale bar: 0.2 mm.
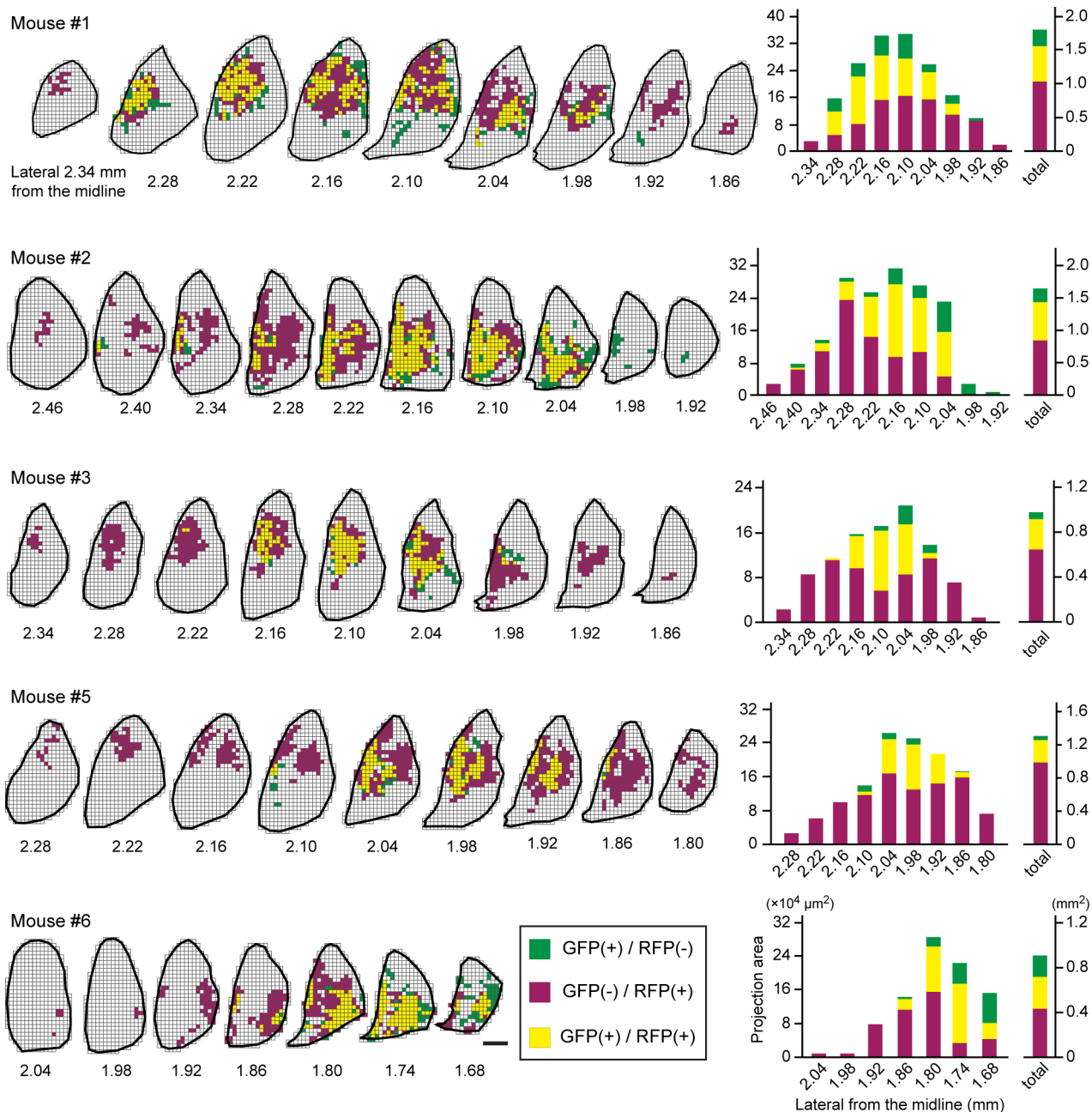
Figure S5. Area analysis of the distribution of GFP+ and/or RFP+ axon fibers in the GPe, Related to Figure 6. Green, red, and yellow boxes indicate the area containing the fibers that were positive for GFP only, RFP only, and both GFP and RFP, respectively. The number of each box type was counted in parasagittal sections and converted to the area $[\times10^4\ \mu m^2]$. Each of these areas $[\times10^4\ \mu m^2]$ and their sums $[mm^2]$ are represented by a bar graph. Note that the 'total' here is the sum of the areas calculated for the analyzed sections and does not represent the total number of actual axon projection ranges.

Transparent Methods

Animals

All procedures involving animals were in accordance with the National Institutes of Health Guide for the Care and Use of Laboratory Animals. The experiments were approved by the Committees for Animal Care and Use and those for Recombinant DNA Study at Kyoto University and Juntendo University. Drd1-Cre BAC transgenic male mice (8–16 weeks; n = 15 in total; FK150Gsat/Mmucd; stock number: 029178-UCD; MMRRC, UC Davis) (Gong et al., 2007) were used in the present study. Mice were maintained under a 12-h light/dark cycle and were provided *ad libitum* access to food and water. All efforts were made to minimize animal suffering and the number of animals used.

Fixation and tissue preparation

Drd1-Cre transgenic mice were deeply anesthetized by intraperitoneal injection of a three-drug mixture of medetomidine (0.3 mg/kg; Nihon Zenyaku Kogyo, Koriyama, Japan), midazolam (6 mg/kg; Sandoz, Tokyo, Japan), and butorphanol (Vetorphal®; 5 mg/kg; Meiji Seika Pharma, Tokyo, Japan). Mice were then perfused transcardially with 20 mL of 5 mM phosphate-buffered 0.9% saline (PBS; pH 7.4), followed by perfusion for 3 minutes with the same volume of 4% formaldehyde (16223-55; Nacalai Tesque, Kyoto, Japan), 75%-saturated picric acid (27925-25; Nacalai Tesque), and 0.1 M Na_2HPO_4 (adjusted to pH 7.2 with NaOH). The brains were removed and post-fixed overnight at 4ºC with the same fixative. After cryoprotection with 30% sucrose in 0.1 M sodium phosphate buffer (PB; pH 7.4), the brains were cut into 20-µm-thick sagittal sections on a freezing microtome (SM2000R; Leica Biosystems, Wetzlar, Germany). Sections were collected in 6 bottles containing 0.02% sodium azide in PBS and stored at 4°C until use for free-floating immunostaining. The shrinkage effect due to chemical fixation was not corrected for comparison of soma and axon distributions between dMSNs and iMSNs. When we measured the maximum lengths of the GPe along the rostrocaudal and dorsoventral planes, the GPe size changed by about 4% (rostrocaudal, 1.15 ± 0.03 mm; dorsoventral, 1.39 ± 0.04 mm; mean $\pm$ SD; n = 6 mice). For the analysis of topography in Figures 7 and 8, we normalized the fixed samples to the brain atlas (Franklin and Paxinos, 2007) to correct the shrinkage effect and determine the

coordinates with ADOBE ILLUSTRATOR CS3 software (Adobe Systems, San Jose, CA).

Production of AAV vector

We used the flip-excision (FLEX) switch (Schnutgen et al., 2003) to express GFP or RFP in the presence or absence of Cre. The sequence of a reporter protein that contained mRFP1 (Campbell et al., 2002) and inverted EGFP (Clontech, Palo Alto, CA), both tagged with a membrane-targeting signal, palmitoylation signal (Furuta et al., 2001; Kameda et al., 2008; Moriyoshi et al., 1996; Okada et al., 1999; Tamamaki et al., 2000) derived from GAP-43 N-terminus, was amplified by overlap PCR (primer set P1–P4; Table S1). The PCR product, pR-pG(r), was inserted into the *EcoRI*/*SalI* sites of pSK-hFLEX (Sohn et al., 2017), resulting in pSK-FLEX-[pR-pG(r)]. The *BamHI*-to-*MluI* fragment from the plasmid was complementarily inserted into the *MluI*/*BamHI* sites of an entry vector, p1A-TGB(r) (Hioki et al., 2009). Subsequently, we amplified the enhanced human synapsin I promoter (E/SYN) (Hioki et al., 2007) by PCR (primer set P5/P6; Table S1) and inserted the PCR product into the *XhoI*/*BamHI* sites of the plasmid, resulting in p1A-E/SYN-FLEX-[pR-pG(r)]. The entry vector was finally converted to pAAV2-E/SYN-FLEX-[pR-pG(r)] by homologous recombination with pAAV2-DEST(r) (Sohn et al., 2017) using LR clonase II (11791020; Thermo Fisher Scientific, Waltham, MA).

Production and purification of AAV vector particles were performed as reported previously (Hamamoto et al., 2017; Kataoka et al., 2014; Suzuki et al., 2015). Briefly, pAAV2-E/SYN-FLEX-[pR-pG(r)] and two helper plasmids, pBSIISK-R2C1 (Sohn et al., 2017) and pHelper (28060929; Stratagene, La Jolla, CA), were co-transfected into HEK293T cells using polyethylenimine (23966; Polysciences, Inc., Warrington, PA). Virus particles were extracted by three cycles of freeze-and-thawing, purified from the crude lysate of the cells by ultracentrifugation with OptiPrep (1114542; Axis-Shield, Oslo, Norway), and then concentrated by ultrafiltration with Amicon Ultra-15 (NMWL 50K; Merck Millipore, Darmstadt, Germany). The virus titer was adjusted to 1.0×10^{11} infectious units/mL (IFU/mL) with Dulbecco's phosphate-buffered saline (14249-95; Nacalai Tesque) containing 0.001 % Pluronic F-68 (24040032; Thermo Fisher Scientific). The virus solution was stored in aliquots at −80ºC until use for delivery to brain tissues.

Virus injection

Drd1-Cre transgenic male mice were deeply anesthetized by intraperitoneal injection of a mixture of medetomidine (0.3 mg/kg), midazolam (4 mg/kg), and butorphanol (5 mg/kg) and placed in a stereotaxic apparatus. We injected 0.2 µL of the virus solution into the CPu of Drd1-Cre mice by pressure through a glass micropipette attached to Picospritzer III (Parker Hannifin Corporation, Cleveland, OH). The injection coordinates were as follows: 0.5–1.0 mm anterior to bregma, 1.8–2.4 mm lateral to the midline, and 2.3–2.5 mm ventral to the brain surface. After the surgery, the mice received an intraperitoneal injection of atipamezole (Antisedan®; 1.5 mg/kg; Orion Corporation, Espoo, Finland) and recovered from anesthesia in about 15 minutes. The mice were maintained in specific pathogen-free conditions under a 12-hour light/dark cycle (light: 08:00–20:00) with *ad libitum* access to food and water for one week after AAV injections; subsequently, they were subjected to transcardial perfusion as described above.

Immunofluorescence labeling

After blocking with 10% normal donkey serum (NDS; S30-100ML; Merck Millipore) in PBS containing 0.3% Triton-X (35501-15; Nacalai Tesque) (PBS-X) for 30 minutes, the brain sections were incubated overnight with one of the following mixtures: (1) 1:5000 diluted rabbit anti-Cre recombinase antibody (69050; Merck Millipore) and 1 µg/mL of affinity-purified guinea-pig anti-PPD antibody (Lee et al., 1997); (2) 1:5000 diluted rabbit anti-Cre recombinase antibody and 1 µg/mL of affinity-purified guinea-pig anti-PPE antibody (Lee et al., 1997); (3) 20 µg/mL of chicken anti-GFP antibody (GFP-1020; Aves Labs, Tigard, OR) and 1 µg/mL of affinity-purified guinea-pig anti-PPD; (4) 1 µg/mL of affinity-purified rabbit anti-mRFP antibody (Hioki et al., 2010) and 1 µg/mL of affinity-purified guinea-pig anti PPE; or (5) 1:1000 diluted mouse anti-calbindin antibody (C9848; Merck Millipore), 20 µg/mL of chicken anti-GFP antibody, and 1 µg/mL of affinity-purified rabbit anti-mRFP antibody. The free-floating incubation was performed at 20–25ºC in PBS-X containing 0.12% λ-carrageenan (035-09693; Wako Chemicals, Osaka, Japan) and 1% NDS (PBS-XCD). Subsequently, the sections were incubated for 2 hours with one of the following mixtures: (a) 5 µg/mL of

AlexaFluor (AF) 488-conjugated antibody against rabbit IgG (A-11034; Thermo Fisher Scientific) and 5 μg/mL of AF568-conjugated antibody against guinea-pig IgG (A-11075; Thermo Fisher Scientific) for the primary antibody mixtures (1) and (2); (b) 5 μg/mL of AF488-conjugated antibody against chicken IgY (A-11039; Thermo Fisher Scientific) and 5 μg/mL of AF647-conjugated antibody against guinea-pig IgG (A-21450; Thermo Fisher Scientific) for the primary antibody mixture (3); (c) 5 μg/mL of AF568-conjugated antibody against rabbit IgG (A-11011; Thermo Fisher Scientific) and 5 μg/mL of AF647-conjugated antibody against guinea-pig IgG for the primary antibody mixture (4); or (d) 5 μg/mL of AF647-conjugated antibody against mouse IgG (A-21236; Thermo Fisher Scientific), 5 μg/mL of AF488-conjugated antibody against chicken IgY and 5 μg/mL of AF568-conjugated antibody against rabbit IgG for the primary antibody mixture (5). The sections were mounted onto gelatinized glass slides and coverslipped with 50% glycerol and 2.5% 1,4-diazabicyclo [2.2.2] octane (049-25712; Wako Chemical) in PBS.

The 3D image stacks were acquired under a TCS SP8 confocal laser scanning microscope (Leica Microsystems) equipped with a 25× water-immersion objective lens (HCX PL APO; NA = 0.95; Leica) and the pinhole set at 5.0 airy disk units. AF488, AF568, or AF647 were excited with 488, 543, or 643 nm laser beams and observed through 500–580, 590–650, or 660–850 nm emission prism windows, respectively. Images were then deconvolved with Huygens Essential software (version 3.8; Scientific Volume Imaging, Hilversum, Netherlands). Finally, the stack images were projected using ImageJ software (ver. 1.52i; National Institutes of Health).

Immunoperoxidase staining

All free-floating incubations were performed at 20–25ºC. After sectioning the brains with a freezing microtome, sections were serially collected in 6 bottles, as described above. The sections in the first and fourth bottles were incubated with 0.1 μg/mL of affinity-purified anti-GFP rabbit antibody (Nakamura et al., 2008; Tamamaki et al., 2000); those in the second and fifth bottles were incubated with 0.1 μg/mL of affinity-purified anti-mRFP rabbit antibody. The sections were incubated with a secondary antibody, biotinylated goat anti-rabbit IgG (BA-1000; Vector Laboratories, Burlingame, CA), in PBS-XCD for 2 hours, and then for 1 hour

with avidin-biotinylated peroxidase complex (1:100; ABC-elite; Vector Laboratories) in PBS-X. The sections were then incubated for 30 minutes in biotinylated tyramine (BT)-glucose oxidase (GO) reaction mixture containing 1.25 μM BT, 3 μg/mL of GO (16831-14; Nacalai Tesque), 2 mg/mL of beta-D-glucose (16804-32; Nacalai Tesque), and 1% bovine serum albumin (BSA; 01863-77; Nacalai Tesque) in 0.1 M PB (pH 7.4) (Furuta et al., 2009; Hioki et al., 2016; Kuramoto et al., 2009). The BT-GO method enables amplification of signals by the deposition of biotin molecules via the peroxidase activity of avidin-biotinylated peroxidase complex. Subsequently, the sections were again incubated for 1 hour with ABC in PBS-X. The bound peroxidase was finally developed by reaction for 30–60 minutes with 0.02% diaminobenzidine (DAB)-4HCl (347-00904; Dojindo, Kumamoto, Japan) and 0.0001% H_2O_2 in 50 mM Tris-HCl, pH 7.6. All stained sections were serially mounted onto gelatinized glass slides, dried, serially dehydrated in ethanol, cleared in xylene, and coverslipped with NEW MX mounting medium (FX00500; Matsunami, Kishiwada, Japan).

Axon tracing

DAB-stained sections were automatically captured as large color images using a TOCO digital slide scanner (CLARO, Aomori, Japan) equipped with a 10x objective lens (EC Plan-Neo fluar; NA, 0.30; Zeiss, Oberkochen, Germany). On the images, we traced and digitized the axonal fibers with a pen tablet (Bamboo Tablet; Wacom Corporation, Saitama, Japan) and ADOBE ILLUSTRATOR CS3 software.

Quantification and statistical analysis

To estimate the density of axon fibers, we converted the data of axon tracing from vector type to raster type using ADOBE PHOTOSHOP CS3 (Adobe Systems). After subdividing the GPe into 40 μm × 40 μm boxes, the density of GFP+ or RFP+ axon fibers in each box was determined using the histogram tool (ADOBE PHOTOSHOP CS3). The results were exported to Microsoft Excel 2013 software (Microsoft, Redmond, WA), and the heat map images were depicted in ADOBE ILLUSTRATOR CS3 software.

We modeled the density of axon fibers in a sample with two Gaussian distributions. The boxes were used as data points, each of which was weighted by its axonal density. Since the number of data points along the z-

axis (across slices) was much less than that along the x- and y-axes (within slices), we augmented data by copying each data point to 20 μm above and 20 μm below the slice containing it. For each sample, a total of 100 initial conditions were used to obtain the best fit of the model using mclust (Scrucca et al., 2016). The center of each Gaussian distribution on the rostral and caudal portions of the GPe was determined and named as Arborizations #1 and #2, respectively. The distances between two GFP+ and RFP+ arborizations (G1-G2 and R1-R2) and distances between overlapping GFP+ and RFP+ arborizations (G1-R1 and G2-R2) were compared by using the Kolmogorov-Smirnov test with R package software (version 3.4.1; R Development Core Team). We analyzed the distribution of axon fibers of dMSNs and iMSNs. After subdividing the GPe as described above, boxes containing GFP+ and/or RFP+ fibers were plotted in the parasagittal plane. The number of each box type was counted and then converted to the area. Finally, the proportion of boxes positive for GFP only, RFP only, or both GFP and RFP was calculated for all sections.

To examine the topographical projections, 3D coordinates of the infected cells were first determined by referring to the brain atlas (Franklin and Paxinos, 2007). Using the coordinates, the center of gravity of the infection site was calculated in each injection experiment. The centers of the infection sites and the centers of the arborizations were then plotted in the rostrocaudal, dorsoventral, and mediolateral planes. Linear regression analysis was performed using Microsoft Excel 2013 software.

The GPe was outlined in accordance with the cytoarchitecture, and CB-rich and CB-poor regions were distinguished as described above. The immunofluorescence intensities of GFP and RFP were measured using ImageJ software. The total intensities of GFP and RFP in the two regions were normalized to 1 arbitrary unit in each mouse, and the percentage of the intensities in each region was calculated. Multiple comparison tests were performed using one-way ANOVA followed by Tukey's *post hoc* test in R package software.

Supplemental References

Campbell, R.E., Tour, O., Palmer, A.E., Steinbach, P.A., Baird, G.S., Zacharias, D.A., and Tsien, R.Y. (2002). A monomeric red fluorescent protein. Proc Natl Acad Sci U S A 99, 7877-7882.

Franklin, K.B.J., and Paxinos, G. (2007). Paxinos and Franklin's The mouse brain in stereotaxic coordinates.

Furuta, T., Kaneko, T., and Deschenes, M. (2009). Septal neurons in barrel cortex derive their receptive field input from the lemniscal pathway. J Neurosci 29, 4089-4095.

Furuta, T., Tomioka, R., Taki, K., Nakamura, K., Tamamaki, N., and Kaneko, T. (2001). In vivo transduction of central neurons using recombinant Sindbis virus: Golgi-like labeling of dendrites and axons with membrane-targeted fluorescent proteins. J Histochem Cytochem 49, 1497-1508.

Gong, S., Doughty, M., Harbaugh, C.R., Cummins, A., Hatten, M.E., Heintz, N., and Gerfen, C.R. (2007). Targeting Cre recombinase to specific neuron populations with bacterial artificial chromosome constructs. J Neurosci 27, 9817-9823.

Hamamoto, M., Kiyokage, E., Sohn, J., Hioki, H., Harada, T., and Toida, K. (2017). Structural basis for cholinergic regulation of neural circuits in the mouse olfactory bulb. J Comp Neurol 525, 574-591.

Hioki, H., Kameda, H., Nakamura, H., Okunomiya, T., Ohira, K., Nakamura, K., Kuroda, M., Furuta, T., and Kaneko, T. (2007). Efficient gene transduction of neurons by lentivirus with enhanced neuron-specific promoters. Gene Ther 14, 872-882.

Hioki, H., Kuramoto, E., Konno, M., Kameda, H., Takahashi, Y., Nakano, T., Nakamura, K.C., and Kaneko, T. (2009). High-level transgene expression in neurons by lentivirus with Tet-Off system. Neurosci Res 63, 149-154.

Hioki, H., Nakamura, H., and Furuta, T. (2016). Application of Virus Vectors for Anterograde Tract-Tracing and Single-Neuron Labeling Studies. In Receptor and Ion Channel Detection in the Brain, R. Luján, and F. Ciruela, eds. (New York, NY: Humana Press), pp. 247-266.

Hioki, H., Nakamura, H., Ma, Y.F., Konno, M., Hayakawa, T., Nakamura, K.C., Fujiyama, F., and Kaneko, T. (2010). Vesicular glutamate transporter 3-expressing nonserotonergic projection neurons constitute a subregion in the rat midbrain raphe nuclei. J Comp Neurol 518, 668-686.

Kameda, H., Furuta, T., Matsuda, W., Ohira, K., Nakamura, K., Hioki, H., and Kaneko, T. (2008). Targeting green fluorescent protein to dendritic membrane in central neurons. Neurosci Res 61, 79-91.

Kataoka, N., Hioki, H., Kaneko, T., and Nakamura, K. (2014). Psychological stress activates a dorsomedial hypothalamus-medullary raphe circuit driving brown adipose tissue thermogenesis and hyperthermia. Cell Metab 20, 346-358.

Kuramoto, E., Furuta, T., Nakamura, K.C., Unzai, T., Hioki, H., and Kaneko, T. (2009). Two types of thalamocortical projections from the motor thalamic nuclei of the rat: a single neuron-tracing study using viral vectors. Cereb Cortex 19, 2065-2077.

Lee, T., Kaneko, T., Taki, K., and Mizuno, N. (1997). Preprodynorphin-, preproenkephalin-, and

preprotachykinin-expressing neurons in the rat neostriatum: an analysis by immunocytochemistry and retrograde tracing. J Comp Neurol 386, 229-244.

Moriyoshi, K., Richards, L.J., Akazawa, C., O'Leary, D.D., and Nakanishi, S. (1996). Labeling neural cells using adenoviral gene transfer of membrane-targeted GFP. Neuron 16, 255-260.

Nakamura, K.C., Kameda, H., Koshimizu, Y., Yanagawa, Y., and Kaneko, T. (2008). Production and histological application of affinity-purified antibodies to heat-denatured green fluorescent protein. J Histochem Cytochem 56, 647-657.

Okada, A., Lansford, R., Weimann, J.M., Fraser, S.E., and McConnell, S.K. (1999). Imaging cells in the developing nervous system with retrovirus expressing modified green fluorescent protein. Exp Neurol 156, 394-406.

Schnutgen, F., Doerflinger, N., Calleja, C., Wendling, O., Chambon, P., and Ghyselinck, N.B. (2003). A directional strategy for monitoring Cre-mediated recombination at the cellular level in the mouse. Nat Biotechnol 21, 562-565.

Scrucca, L., Fop, M., Murphy, T.B., and Raftery, A.E. (2016). mclust 5: Clustering, Classification and Density Estimation Using Gaussian Finite Mixture Models. R j 8, 289-317.

Sohn, J., Takahashi, M., Okamoto, S., Ishida, Y., Furuta, T., and Hioki, H. (2017). A Single Vector Platform for High-Level Gene Transduction of Central Neurons: Adeno-Associated Virus Vector Equipped with the Tet-Off System. PLoS One 12, e0169611.

Suzuki, Y., Kiyokage, E., Sohn, J., Hioki, H., and Toida, K. (2015). Structural basis for serotonergic regulation of neural circuits in the mouse olfactory bulb. J Comp Neurol 523, 262-280.

Tamamaki, N., Nakamura, K., Furuta, T., Asamoto, K., and Kaneko, T. (2000). Neurons in Golgi-stain-like images revealed by GFP-adenovirus infection in vivo. Neurosci Res 38, 231-236.